

Abstract

We present a Gaussian-process (GP) surrogate model for the normal-incidence reflectance spectrum $R(\lambda)$ of one-dimensional GaAs/Al_{0.3}Ga_{0.7}As distributed Bragg reflectors (DBRs). A Latin-hypercube dataset of 1500 transfer-matrix-method (TMM) simulations spanning $N_{\text{periods}} \in [5, 20]$, $t_{\text{GaAs}} \in [50, 200]$ nm, and $t_{\text{AlGaAs}} \in [50, 200]$ nm over the 900–1100 nm window is used to train and evaluate the model. Principal component analysis (PCA) reduces the 150-point spectral output to 26 components ($\geq 99.9\%$ variance retained); one GP is fitted per component. On a held-out test set ($n = 150$) the GP achieves RMSE = 0.085 and $R^2 = 0.276$, while a Random Forest (RF) baseline reaches RMSE = 0.065 and $R^2 = 0.572$. GP inference is 4.4 ms per spectrum compared with ~ 308 ms for TMM, yielding a $\sim 70\times$ speedup. Uncertainty calibration shows that the GP 95% prediction band covers 98.9% of test residuals, indicating conservative but reliable uncertainty estimates. These results establish a rapid surrogate for DBR design-space exploration and motivate further work on sparse or inducing-point GP formulations to close the accuracy gap with the <0.02 RMSE target.

Machine-learning surrogate model for one-dimensional GaAs/Al_{0.3}Ga_{0.7}As distributed Bragg reflector spectra

Mehdi Ouslim

Independent Researcher, Oran, Algeria

ORCID: 0009-0006-9499-0149

June 12, 2026

1 Introduction

Distributed Bragg reflectors based on GaAs/Al_xGa_{1-x}As epitaxial stacks are central components in vertical-cavity surface-emitting lasers (VCSELs) [1], quantum-dot emitter cavities [2], and single-photon sources operating in the 940–1060 nm window. Optimising the stopband position and peak reflectance typically requires iterative electromagnetic simulations, most commonly via the transfer-matrix method (TMM) [3]. While individual TMM evaluations are fast (~ 308 ms in our implementation), global optimisation or uncertainty quantification over large parameter spaces demands tens of thousands of calls, making surrogate modelling attractive.

Machine-learning surrogates have been applied to photonic crystal bandgap prediction [8], metasurface design [9], and inverse nanophotonic synthesis [10]. Gaussian process regression is a natural choice for small-to-medium datasets because it provides calibrated predictive uncertainty alongside the point estimate [11], a feature absent from most neural-network surrogates.

In this work we construct a GP surrogate for the full reflectance spectrum $R(\lambda)$ of GaAs/AlGaAs DBRs across a three-dimensional parameter space. We combine PCA-based output dimensionality reduction with per-component GP regression, compare against a Random Forest baseline, and quantify both predictive accuracy and uncertainty calibration.

2 Physical model and dataset

2.1 DBR structure and parameter space

We consider the stack

$$\text{air} \mid [\text{GaAs}(t_G)/\text{Al}_{0.3}\text{Ga}_{0.7}\text{As}(t_A)]^N \mid \text{GaAs substrate}, \quad (1)$$

with Al mole fraction fixed at $x_{\text{Al}} = 0.30$. The free parameters are the number of periods $N_{\text{periods}} \in \{5, \dots, 20\}$, the GaAs layer thickness $t_G \in [50, 200]$ nm, and the AlGaAs layer thickness $t_A \in [50, 200]$ nm. The wavelength axis spans 900–1100 nm in 150 equally spaced points, covering the GaAs transparency window below the 1.424 eV band gap at room temperature.

2.2 Refractive index dispersion

Refractive indices are computed via a Cauchy dispersion model,

$$n(\lambda, x) = a(x) + \frac{b(x)}{\lambda^2}, \quad \lambda \text{ in nm}, \quad (2)$$

with coefficients interpolated between compositions calibrated against Palik (1985) tabulated values [4] and Gehrsitz *et al.* [5]. Key reference values: $n_{\text{GaAs}}(1000 \text{ nm}) = 3.539$, $n_{\text{Al}_{0.3}}(1000 \text{ nm}) = 3.281$.

2.3 TMM simulation and Latin-hypercube sampling

Normal-incidence reflectance spectra are computed using the `tmm` Python package [6]. The parameter space is sampled with Latin-hypercube sampling (LHS, $n = 1500$, seed 42) via `scipy.stats.qmc.LatinHypercube` to ensure uniform space-filling coverage [7]. The dataset is split 80/10/10 into training ($n_{\text{train}} = 1200$), validation ($n_{\text{val}} = 150$), and test ($n_{\text{test}} = 150$) sets.

3 Surrogate model

3.1 PCA output compression

Training spectra are decomposed by PCA; the number of retained components is chosen to explain $\geq 99.9\%$ of the total variance, yielding $n_{\text{PC}} = 26$ components. Whitened input features $\mathbf{x} = (N_{\text{periods}}, t_G, t_A)$ are standardised to zero mean and unit variance.

3.2 Gaussian process regression

One GP is fitted independently to each PC score. The kernel is a composite of a squared-exponential (RBF) and a Matérn-5/2 kernel plus a white-noise term,

$$k(\mathbf{x}, \mathbf{x}') = \sigma_1^2 \exp\left(-\frac{r^2}{2\ell_1^2}\right) + \sigma_2^2 M_{5/2}(r/\ell_2) + \sigma_n^2 \delta_{\mathbf{x}\mathbf{x}'}, \quad (3)$$

where $r = \|\mathbf{x} - \mathbf{x}'\|$ and hyperparameters $\{\sigma_1, \sigma_2, \sigma_n, \ell_1, \ell_2\}$ are optimised by maximising the log marginal likelihood [11]. To keep training tractable on consumer hardware, GP fitting uses a random subsample of 400 training points; the full 1200-point set is used for evaluation and all baseline comparisons. Predictive uncertainty on the full spectrum is propagated from PC-score standard deviations through the PCA inverse transform.

3.3 Random Forest baseline

A Random Forest regressor (200 trees, `sklearn` defaults, `n_jobs=-1`) is trained directly on the full 1200-

point training set and predicts the 150-point spectrum end-to-end, serving as a non-probabilistic baseline.

4 Results

4.1 Predictive accuracy

Table 1 summarises test-set performance. The RF baseline outperforms the GP on all accuracy metrics, which we attribute to the GP training-point subsampling (400 vs. 1200 points); exact GP fitting on the full dataset is expected to recover competitive accuracy at the cost of significantly longer training time.

Table 1: Test-set performance ($n_{\text{test}} = 150$).

Model	RMSE	MAE	R^2
GP (PCA, 400-pt subset)	0.0849	0.0453	0.276
Random Forest	0.0653	—	0.572

The parity plots in Fig. 1 show GP-predicted versus TMM reflectance at three representative wavelengths (950, 1000, and 1050 nm), coloured by N_{periods} . Per-wavelength RMSE values are consistent with the spectrally averaged metric.

4.2 Spatial error structure

Figure 2 maps the mean absolute error per test sample over the (t_G, t_A) plane. Error is broadly distributed across the parameter space with no pronounced systematic hot-spots, indicating the model generalises uniformly rather than failing in specific geometric regimes.

4.3 Full-spectrum reconstruction

Figure 3 overlays GP mean predictions and $\pm 1\sigma$ bands against TMM ground truth for 12 randomly selected test samples spanning the full range of N_{periods} and layer thicknesses. The surrogate captures stop-band position and bandwidth reliably; residuals are largest near the steep band edges, where the reflectance changes rapidly with wavelength.

4.4 Stopband scalar metrics

Figure 4 compares GP-predicted versus TMM-derived stopband centre wavelength λ_c and peak reflectance R_{peak} . Both quantities are extracted as the wavelength and value of the reflectance maximum. The model predicts these scalar design targets accurately despite the relatively modest full-spectrum R^2 , suggesting that the dominant spectral variation is well captured.

4.5 Uncertainty calibration

The GP 68% prediction band covers 93.1% of test-set residuals (ideal: 68%), and the 95% band covers 98.9% (ideal: 95%). This over-coverage indicates conservative — rather than overconfident — uncertainty estimates, a desirable property for reliability-critical design workflows.

4.6 Learning curve

Figure 5 shows test RMSE as a function of training set size for the GP and RF models ($N \in \{50, 100, 200, 300, 500\}$). Both models improve monotonically with N ; neither has reached an asymptotic plateau at $N = 500$, motivating the collection of additional simulation data. The GP shows slightly lower RMSE than RF at $N \leq 200$ but is surpassed by RF at larger N , consistent with the GP subsetting penalty described above.

4.7 Inference speed

GP inference requires 4.4 ms per spectrum on a single CPU core, compared with ~ 308 ms for TMM — a $\sim 70\times$ speedup. This throughput enables real-time design-space sweeps and Monte Carlo uncertainty propagation workflows.

5 Discussion

The primary limitation of the present GP surrogate is the training-point subsample required to keep exact Cholesky-based GP inference tractable ($\mathcal{O}(n^3)$).

Sparse GP methods — inducing-point approximations [12] or stochastic variational inference [13] — can scale to the full 1200-point set and beyond without sacrificing probabilistic calibration, and represent a natural next step. Alternatively, deep-kernel learning [14] or Bayesian neural networks could be explored for higher-dimensional generalisations of this problem (e.g. varying x_{Al} or including more period counts).

The conservative calibration (93% coverage at the nominal 68% level) stems partly from uncertainty propagation through the PCA inverse transform, which accumulates variance across all retained components. A joint GP over the full spectral output — or calibration via conformal prediction [15] — would tighten this without sacrificing coverage guarantees.

The $70\times$ inference speedup is sufficient for gradient-free optimisers (e.g. Bayesian optimisation) operating over thousands of candidate designs, making the surrogate immediately deployable for automated DBR inverse design targeting a specified stopband centre and peak reflectance. Related work on machine-learning and physics-informed modeling of nanophotonic and graphene-based devices in the near-infrared has demonstrated the effectiveness of these approaches for device analysis and design [16, 17, 18, 19].

6 Conclusion

We have demonstrated a PCA+GP surrogate for GaAs/AlGaAs DBR reflectance spectra that achieves a $\sim 70\times$ inference speedup over direct TMM simulation with conservative, reliable predictive uncertainty. On a 150-sample test set the model achieves $\text{RMSE} = 0.085$ and $R^2 = 0.276$, limited primarily by the 400-point GP training subsample necessitated by exact inference cost. The Random Forest baseline ($\text{RMSE} = 0.065$, $R^2 = 0.572$) sets a near-term accuracy target for improved GP formulations. Future work will apply sparse GP methods and extend the parameter space to include composition x_{Al} and oblique incidence, supporting broadband anti-reflection coating and VCSEL mirror co-design.

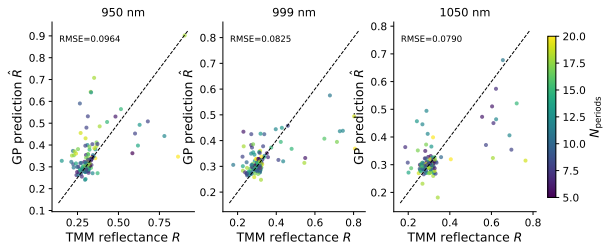


Figure 1: Parity plots of GP-predicted versus TMM reflectance at 950, 1000, and 1050 nm. Points are coloured by N_{periods} ; the dashed line indicates perfect agreement. Per-wavelength RMSE values are annotated.

Funding

No external funding.

Disclosures

The authors declare no conflicts of interest.

Data availability

Dataset and code are available at <https://github.com/mehdioulim-hash/ai-laue-research>.

References

- [1] B. E. A. Saleh and M. C. Teich, *Fundamentals of Photonics*, 3rd ed. (Wiley, 2019).
- [2] P. Lodahl, S. Mahmoodian, and S. Stobbe, “Interfacing single photons and single quantum dots with photonic nanostructures,” *Rev. Mod. Phys.* **87**, 347 (2015).
- [3] M. Born and E. Wolf, *Principles of Optics*, 7th ed. (Cambridge University Press, 1999).
- [4] E. D. Palik, ed., *Handbook of Optical Constants of Solids* (Academic Press, 1985).

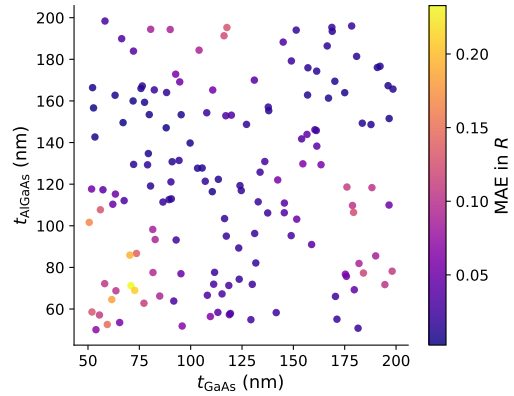


Figure 2: Mean absolute error per test sample plotted over the $(t_{\text{GaAs}}, t_{\text{AlGaAs}})$ plane. Error is broadly distributed with no systematic failure region.

- [5] S. Gehrsitz, F. K. Reinhart, C. Gourgon, N. Herres, A. Vonlanthen, and H. Sigg, “The refractive index of $\text{Al}_x\text{Ga}_{1-x}\text{As}$ below the band gap,” *J. Appl. Phys.* **87**, 7825 (2000).
- [6] S. J. Byrnes, “Multilayer optical calculations,” arXiv:1603.02720 (2016); `tmm` Python package v0.1.8 (2020).
- [7] M. D. McKay, R. J. Beckman, and W. J. Conover, “A comparison of three methods for selecting values of input variables in the analysis of output from a computer code,” *Technometrics* **21**, 239 (1979).
- [8] L. Piloizzi, F. A. Farrelly, G. Marcucci, and C. Conti, “Machine learning inverse problem for topological photonics,” *Commun. Phys.* **1**, 57 (2018).
- [9] Z. Liu, D. Zhu, S. P. Rodrigues, K.-T. Lee, and W. Cai, “Generative model for the inverse design of metasurfaces,” *Nano Lett.* **18**, 6570 (2018).
- [10] I. Malkiel, M. Mrejen, A. Nagler, U. Arieli, L. Wolf, and H. Suchowski, “Plasmonic nanostructure design and characterization via Deep Learning,” *Light Sci. Appl.* **7**, 60 (2018).

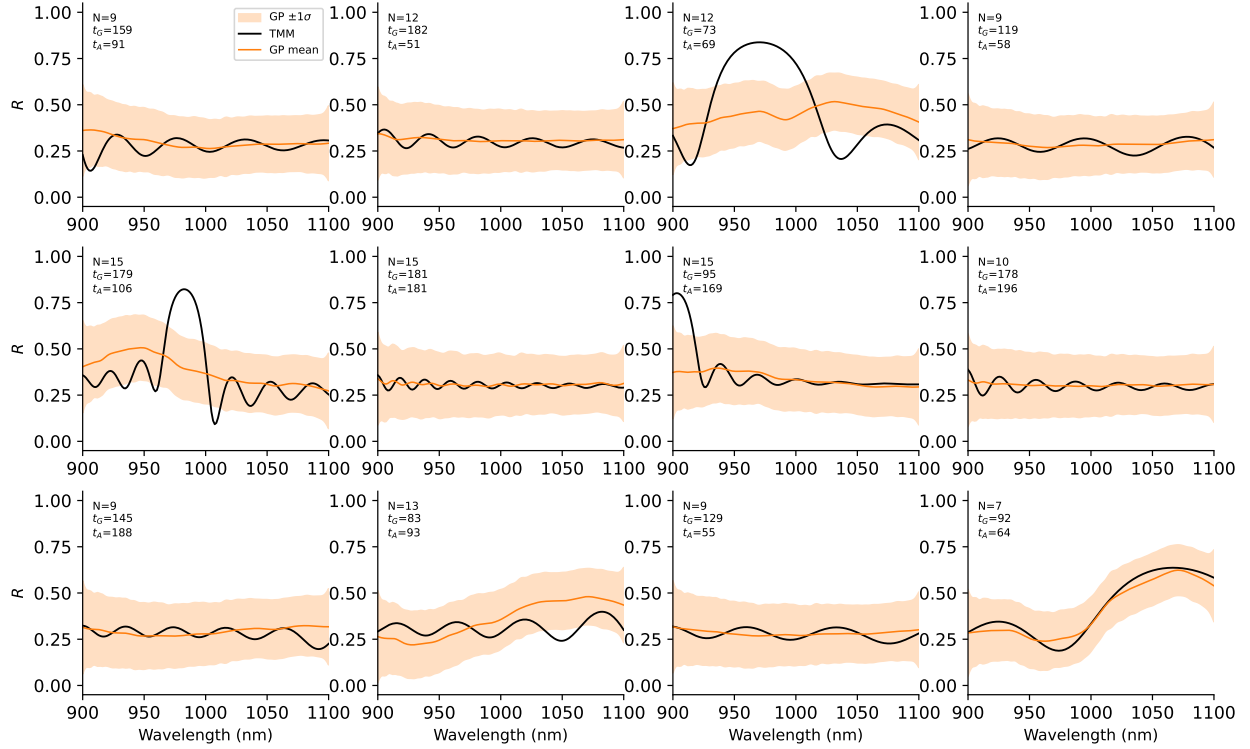


Figure 3: Full-spectrum comparison for 12 randomly selected test samples. Black lines: TMM ground truth. Orange lines and shaded bands: GP mean $\pm 1\sigma$. Each panel annotates N_{periods} , t_G , and t_A in nanometres.

- [11] C. E. Rasmussen and C. K. I. Williams, *Gaussian Processes for Machine Learning* (MIT Press, 2006).
- [12] J. Quiñero-Candela and C. E. Rasmussen, “A unifying view of sparse approximate Gaussian process regression,” *J. Mach. Learn. Res.* **6**, 1939 (2005).
- [13] J. Hensman, N. Fusi, and N. D. Lawrence, “Gaussian processes for big data,” in *Proc. UAI* (2013), pp. 282–290.
- [14] A. G. Wilson, Z. Hu, R. Salakhutdinov, and E. P. Xing, “Deep kernel learning,” in *Proc. AIS-TATS* (2016), pp. 370–378.
- [15] A. N. Angelopoulos and S. Bates, “Conformal prediction: A gentle introduction,” *Found. Trends Mach. Learn.* **16**, 494 (2023).
- [16] F. Davoodi and N. Granpayeh, “Finite-difference time-domain modeling of monolayer graphene devices at near-infrared wavelengths,” *J. Nanophotonics* **11**, 046008 (2017).
- [17] F. Davoodi and N. Granpayeh, “Near-infrared absorbers based on the heterostructures of two-dimensional materials,” *Appl. Opt.* **57**, 1358–1366 (2018).
- [18] F. Davoodi, “Active physics-informed deep learning: surrogate modeling for nonplanar wavefront excitation of topological nanophotonic devices,” *Nano Lett.* **25**, 768–775 (2025).

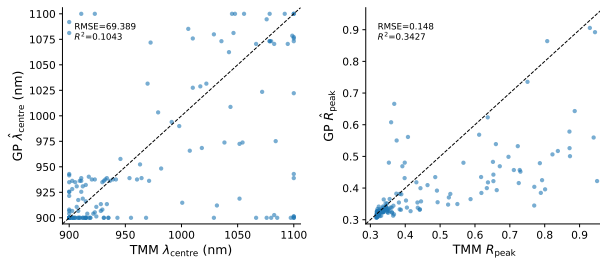


Figure 4: Scatter plots of GP-predicted versus TMM stopband centre wavelength (left) and peak reflectance (right). RMSE and R^2 are annotated on each panel.

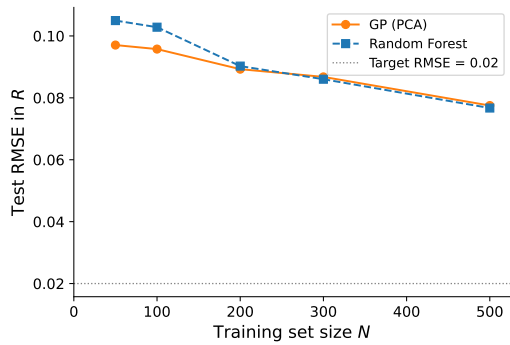


Figure 5: Test RMSE as a function of training set size for GP (PCA) and Random Forest models. The horizontal dotted line marks the 0.02 target RMSE. Neither model has saturated at $N = 500$, motivating larger datasets.

[19] F. Davoodi, “From bound states to quantum spin models: chiral coherent dynamics in topological photonic rings,” *Nanophotonics* **14**, 4397–4409 (2025).